MDPI

Communication

Unraveling the Mechanism of Toughness Fluctuation in Ultra-High-Strength Casing from the Perspective of Crystallography

Zhan Gao [1,2], Xiaoming Dong [2], Jieru Yu [1], Junjie Tang [1], Yishuang Yu [3,*], Liangliang Wei [4,*], Shilong Liu [1,*] and Xuejun Jin [1,3]

1   Institute of Advanced Steels and Materials, School of Materials Science and Engineering, Shanghai Jiao Tong University, Shanghai 200240, China
2   Baosteel Research Institute, Baoshan Iron & Steel Co., Ltd., Shanghai 201900, China
3   School of Biomedical Engineering, Shanghai Jiao Tong University, Shanghai 200240, China
4   Spallation Neutron Source Science Center, Dongguan 523803, China
*   Correspondence: yuyishuang@sjtu.edu.cn (Y.Y.); weill@ihep.ac.cn (L.W.); sliu6@sjtu.edu.cn (S.L.)

Abstract: The microstructure and impact toughness in an ultra-high-strength casing were investigated, attempting to reveal the reason for toughness fluctuations along the casing in terms of crystallography. The morphological structures at the head of the casing are lath bainite, while those at the end are granular bainite and lath bainite. The head exhibits a higher density of high-angle grain boundaries dominated by block boundaries and a higher impact toughness than the end, showing an inhomogeneous microstructure and causing toughness fluctuations in the casing. The higher density of block boundaries in the head resulted from weaker variant selection because of its higher cooling rate than the end. Therefore, the underlying reason for the toughness fluctuations lies in the varying densities of the block boundaries along the casing triggered by uneven cooling.

Keywords: casing; impact toughness; grain boundaries; variant pairing; phase transformation

1. Introduction

Casing, as a key structural component, is widely used in oil and gas exploration [1]. As easily exploitable shallow oil and gas resources are gradually drying up, explorations extend deeper [2]. The harsh service environments in deep oil and gas wells set high requirements for the strength, toughness and performance stability of the casing [3]. Generally, the impact energy of the casing should meet the requirements specified in the API Specification 5CT [1]. However, in some cases the microstructures show no notable differences, but the values of toughness exhibit sharp fluctuations along the casing, which seriously affects the product quality. Toughness fluctuation has increasingly become a bottleneck problem in the production of ultra-high-strength casings [2], and revealing the causes of toughness fluctuation has become a primary problem to be solved.

Toughness fluctuation is mainly related to two factors. One factor is casting defects, such as centerline segregation and casting inclusions [4,5]. Centerline segregation usually causes the formation of band microstructures in the heavy plate, which alters the carbide precipitation behavior and lowers the toughness [6]. Additionally, the casting inclusion, like bifilms and oxide inclusions, may also affect the toughness [7]. The other factor is the microstructural heterogeneity, which is usually induced by an uneven rolling deformation and cooling rate [8–10]. Microstructural heterogeneity usually exists across the thickness direction of heavy plates or along the axis of the steel pipe [11,12]. With the improvement in the casting level, inclusions have been well controlled and are no longer the main cause of toughness fluctuations. For low-alloy casing steel, due to its low Mn content (~1.0 wt.%), the degree of Mn segregation is relatively light. Therefore, the casting defects can be ignored

for casing steel, and microstructural heterogeneity becomes the main reason for toughness fluctuations. An in-depth analysis of the microstructural heterogeneity of casing steel helps to reveal the mechanism of toughness fluctuations.

The microstructures of ultra-high-strength casings are typical lath structures, i.e., martensite/bainite. Lath structures have a hierarchical microstructure which can be categorized into multiscale crystallographic units like prior austenite grains, packets, blocks, sub-blocks and laths [13,14]. A prior austenite grain is composed of several martensite packets with the same habit plane; each packet is then divided into a martensite block, which contains several laths with the same crystallographic orientation. Based on the crystallographic orientation relationship between austenite and bainite, there exist 24 variants transformed from a single austenite grain in low carbon steels, which can be divided into four closed-packed (CP) groups or three Bain groups [15]. Each CP group is made up of six variants sharing the same parallel relationship of closed-packed planes with austenite (CP1: $(111)\gamma//(011)\alpha$, CP2: $(1-11)\gamma//(011)\alpha$, CP3: $(-111)\gamma//(011)\alpha$ and CP4: $(11-1)\gamma//(011)\alpha$). The Bain group consists of eight variants with the same Bain correspondence (B1: $[001]\gamma//[001]\alpha$, B2: $[100]\gamma//[110]\alpha$ and B3: $[010]\gamma//[-110]\alpha$). The boundaries that separate these microstructural units are different in nature and have different misorientation angles across them. In general, prior austenite grain (PAG), packet and block boundaries are high-angle grain boundaries, and lath boundaries are low-angle grain boundaries in martensitic/bainitic structures [13,14,16]. Earlier studies show that refining the PAGs, packets and blocks has a beneficial effect on the enhancement of impact toughness because of the effectiveness in hindering the cleavage crack propagation [17–20]. Studies on the reasons for toughness fluctuations depending on the microstructural heterogeneity from a crystallographic perspective are relatively scarce. Therefore, a crystallographic analysis of the microstructure of the casing can greatly help to elucidate the relationship between crystallographic features and impact toughness, and thus reveal the causes of toughness variation.

In this report, the microstructural heterogeneity in a high-strength casing in terms of crystallography was studied to uncover the mechanism of toughness fluctuation.

2. Materials and Methods

The material investigated in this work is an industrial-produced 155 ksi grade casing with a chemical composition of Fe-0.16C-0.25Si-1.00Mn-2.0(Cr + Mo)-0.09(Nb + V) (wt.%). After hot rolling, the casing was firstly reaustenitized at 900 °C for 2 h, subsequently water-quenched to form lath structures and then tempered at 600 °C for 2 h. These processes were carried out on a continuous industrial production line.

Specimens for the tensile and impact tests and microstructure observation were cut from the head and end of the casing along the rolling direction. The tensile properties were measured at room temperature using flat dog-bone-shaped tensile specimens with a thickness of 12 mm and a gauge section of 50×25 mm^2 according to the GB/T 228.1−2021 specification [21]. The tensile tests were conducted using a universal testing machine (WDW-200, Changchun, China) at a strain rate of 1.0×10^{-3} s^{-1}. Impact toughness was measured at 0 °C using Charpy V-notched impact specimens according to the GB/T 229−2020 standard [22], and the impact tests were carried out on a pendulum impact testing machine (PTM2200−D1, Shenzhen, China). Three specimens were tested for each condition.

The samples for microstructure observation were mounted and mechanically polished. After being etched using 4% nital solution and electropolished using a solution of 10% perchloric acid in ethanol, the samples were characterized by using a TESCAN MIRA3 field emission scanning electron microscope (TESCAN, Brno, Czech Republic) equipped with an Oxford electron backscatter diffraction (EBSD) detector (Oxford Instruments, Oxford, UK). EBSD data were obtained under the following conditions: accelerating voltage, 20 kV; working distance, 15 mm; tilt angle, 70°; step size, 100 nm. HKL Channel 5 software (Oxford Instruments, Oxford, UK) and MATLAB® R2017b software (MathWorks, Natick, MA, USA) were utilized to visualize and digitize the crystallographic features. To reveal the features

of lath structures and carbides, thin foils with a diameter of 3 mm were prepared, and TEM analysis was conducted using a Talos F20 transmission electron microscope (Thermo Fisher, Waltham, MA, USA) operated at an accelerating voltage of 200 kV.

3. Results and Discussion

Figure 1 displays the tensile and impact properties of the head and end samples. The samples exhibit similar tensile properties with a yield strength (YS) of ~1100 MPa, an ultimate tensile strength (UTS) of ~1200 MPa and a total elongation (TEL) of ~21%. However, the end shows a lower 0 °C impact toughness with a reduction of ~41% compared with that of the head, implying that the impact toughness varies along the casing. Obviously, the impact property cannot meet the toughness requirement of a 155 ksi grade casing.
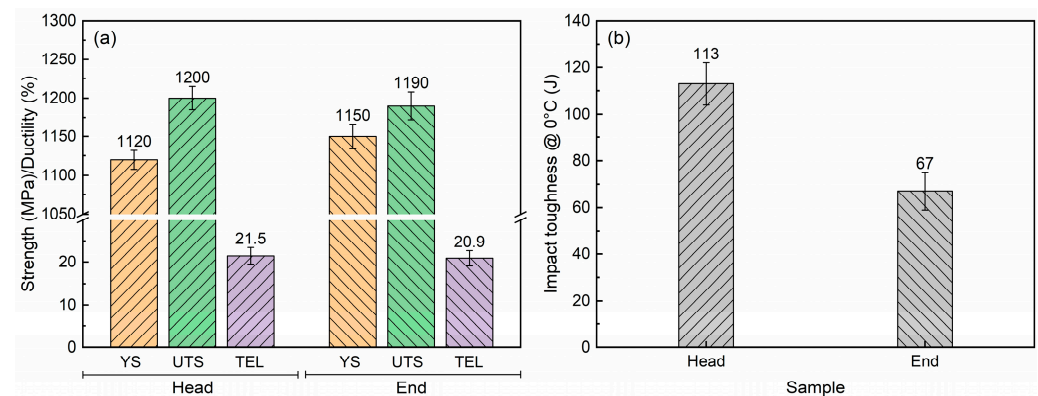

Figure 1. Tensile properties (**a**) and impact toughness (**b**) of the head and end samples. YS, UTS and TEL represent yield strength, ultimate tensile strength and total elongation, respectively.

The SEM micrographs and TEM images of the head and end samples are depicted in Figure 2. The morphological structures at the head are characterized by typical lath bainite (LB), while those at the end are composed of LB with some granular bainite (GB) (Figure 2a,d). In addition, the lath boundary and prior austenite grain boundary (PAGB) are decorated with bright and fine carbides in both samples. In the TEM images (Figure 2b,c,e,f), the width of structures at the head is ~100−200 nm, which is finer compared with that at the end with a width thicker than 200 nm. Carbides with a size of ~50–100 nm can be observed in both samples.
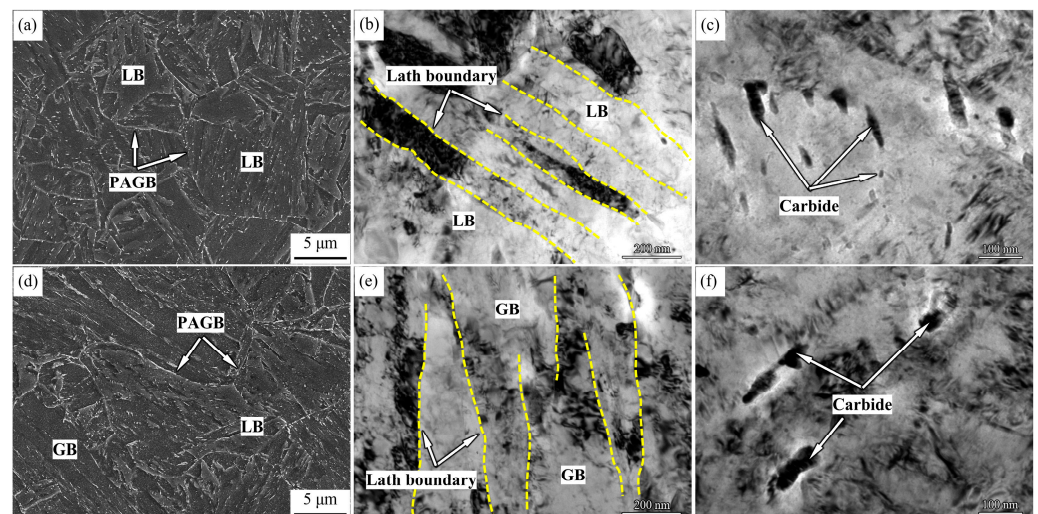

Figure 2. SEM micrographs (**a**,**d**) and TEM images (**b**,**c**,**e**,**f**) depicting the microstructure and carbide distribution in the head (**a**–**c**) and end (**d**–**f**) samples.

Figure 3 displays the band contrast (BC) and inverse pole figure (IPF) maps of the head and end samples. Notable differences in the crystallographic features are observed in the samples. In the BC maps, the boundaries are divided into three types according to the misorientation (θ), i.e., low-angle grain boundaries (LAGBs, $5° < \theta < 15°$), high-angle grain boundaries (HAGBs, $15° < \theta < 45°$) and high-angle grain boundaries (HAGBs, $\theta > 45°$), and are highlighted by white, black and red lines, respectively. Compared with the end, the head exhibits straighter boundaries, most of which are equivalent boundaries of V1/V2 [23]. The head has finer microstructure and higher density of high angle grain boundaries (HAGBs). Previous studies show that toughness is influenced by the distribution of special misorientation angle (SMA) between the {1 0 0} planes and SMA between the {1 1 0} planes [20,24]. The boundaries are vital to the crack initiation and propagation, which are influenced by the boundaries with a high {1 1 0}-SMA and a high {1 0 0}-SMA, respectively. At the stage of crack initiation, boundaries with high {1 1 0}-SMAs will hinder the dislocation gliding, thus lowering the stress concentration at the notch. As a result, larger plastic deformation forms, and more impact energy is obtained. Once a brittle crack forms and begins to propagate, boundaries with high {1 0 0}-SMAs become the main influencing factor by hindering the crack propagation. Boundaries with high {1 0 0}-SMAs are usually HAGBs. Therefore, the boundaries, especially the HAGBs, contribute to the enhancement of impact toughness [20,24–28].
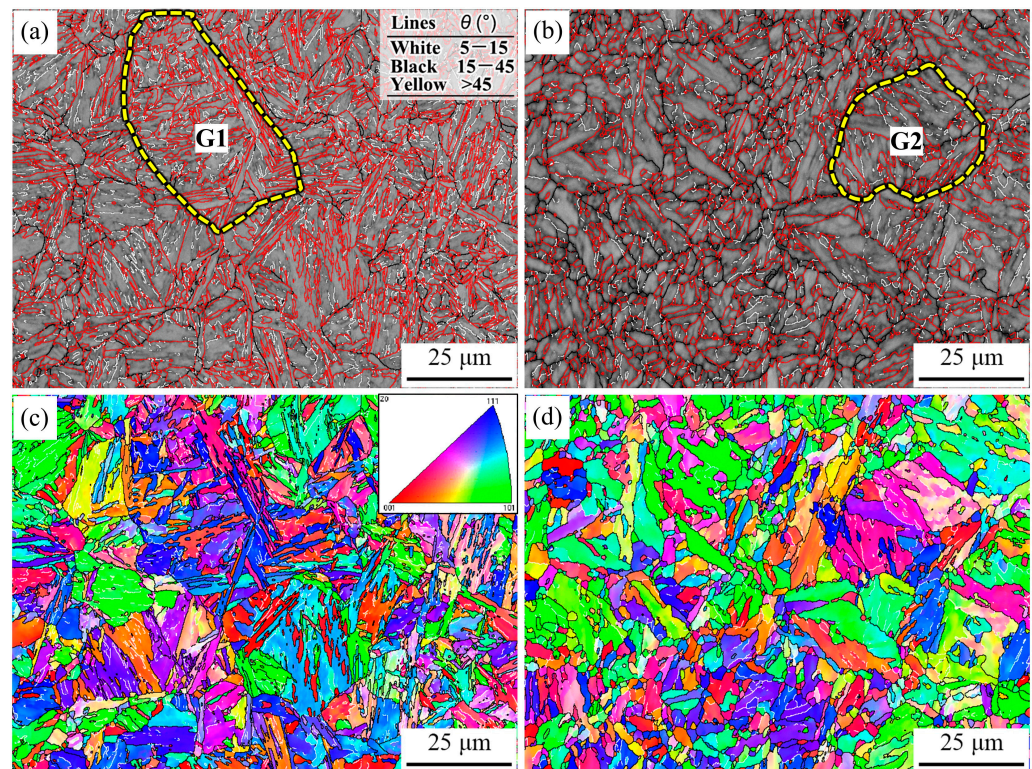

Figure 3. BC (**a**,**b**) and IPF (**c**,**d**) maps depicting the microstructure and boundary distribution in the head (**a**,**c**) and end (**b**,**d**) samples.

To further analyze the microstructural heterogeneity of the samples, an inspection was conducted to visualize and digitize the crystallographic features. Figure 4 shows the structures of representative grains highlighted with yellow dotted lines in Figure 3a,b. One can see from the GB and IPF maps that the G1 grain from the head exhibits a higher density of HAGBs and finer structures than the G2 grain from the end. In this study, the 24 variants transformed from the representative grain were classified as four CP groups and three Bain groups which were highlighted with four and three colors, respectively. It is noticed from the CP and Bain group maps that the boundaries between variants in the same Bain region are LAGBs (white lines), while the boundaries between variants belonging to different Bain

groups are HAGBs (black lines). Interestingly, most of the CP regions in the G1 grain are occupied by different fine Bain groups, implying that variants from distinct Bain groups are preferentially formed. In contrast, the CP regions in the G2 grain are inclined to an arrangement with the same coarse Bain groups, which is detrimental to the formation of HAGBs.
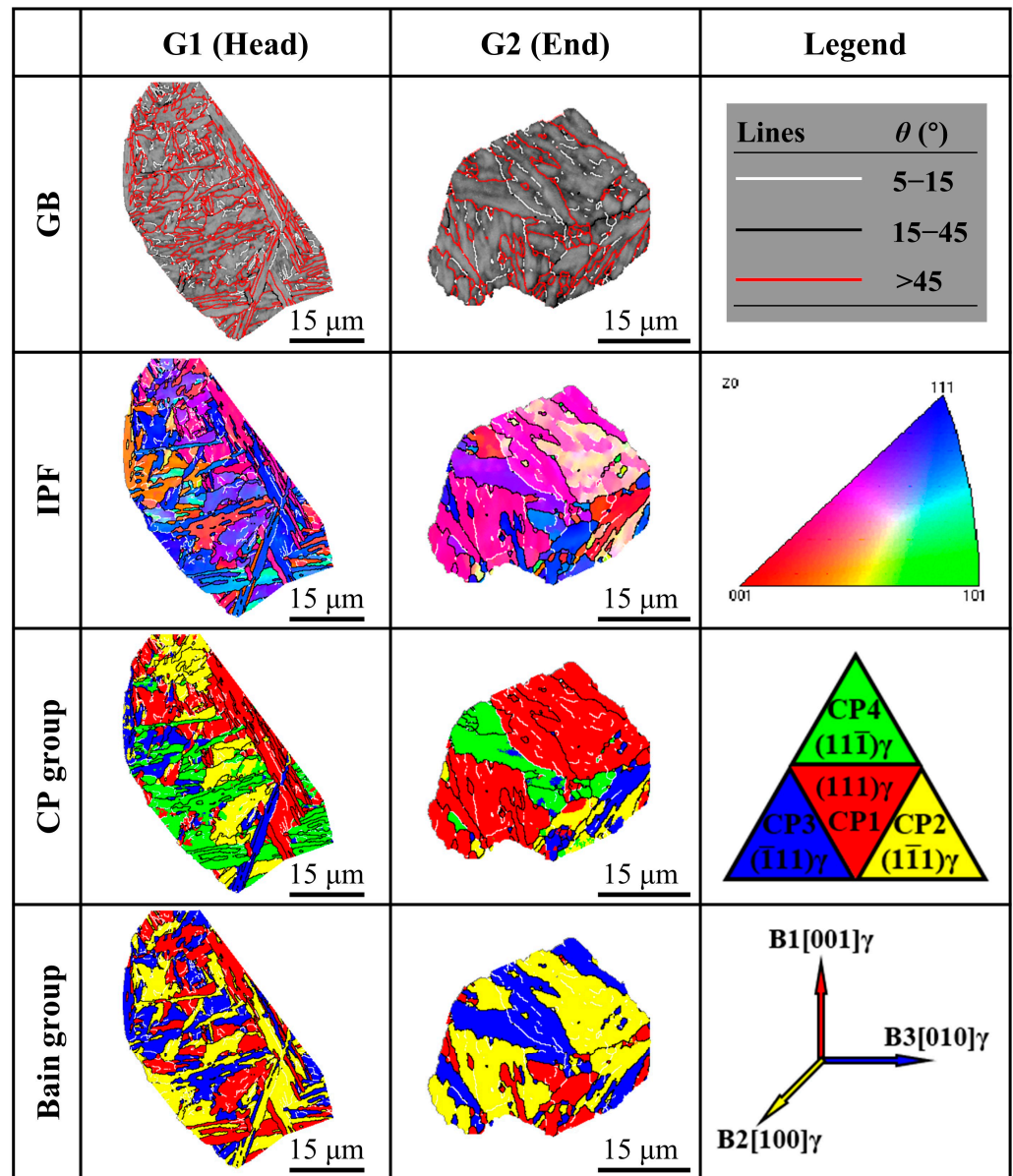

Figure 4. Visualization of the crystallographic features in the representative grains: GB maps, IPF and corresponding CP and Bain maps of the G1 and G2 grains.

The HAGBs and arrangements of CP and Bain groups within the grains are associated with variant selection [29–32]. Based on the actual orientation relationship, the fractions of the variant in the G1 and G2 grains were calculated quantitatively according to the method reported in refs. [33,34], and the results are pictured in Figure 5. Horizontal dash–dot lines stand for the fraction of the random distribution of variants (i.e., 1/24), which denotes that no variant selection occurs. Clearly, a total of 24 variants from V1 to V24 were all formed in both grains. The G1 grain from the head shows a very weak variant selection verified by the random distribution of 24 variants, while the G2 grain from the end formed predominant variants (i.e., V10, V16, V18 and V21), showing a strong variant selection. Previous studies suggest that a high cooling rate can weaken the variant selection and contribute to the

formation of different variants and the refinement of packets and blocks [8,23,35]. In this work, the different variant pairing tendencies in the head and the end resulted from uneven cooling along the casing. It can be inferred that the cooling rate at the head should be higher than that at the end since the variant selection in the head is weaker.
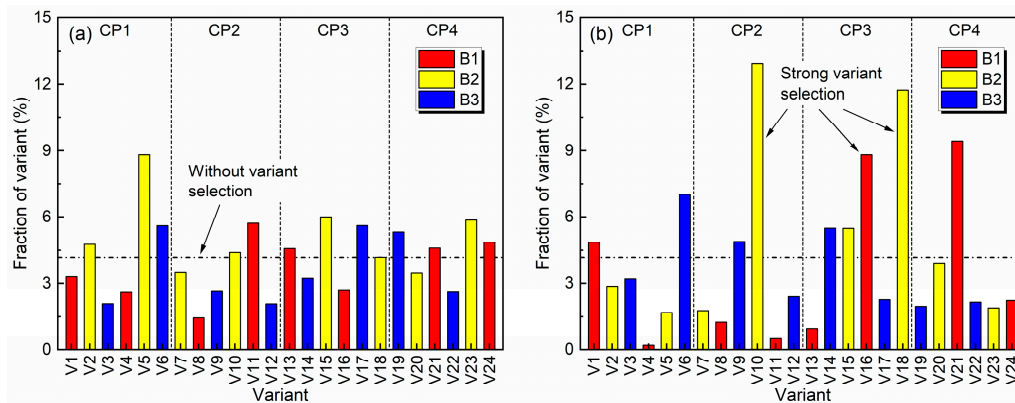

Figure 5. Digitization of the crystallographic features in the representative grains: fractions of the variant in the G1 (**a**) and G2 (**b**) grains.

For better comprehension of the relationship between intervariant boundaries and impact toughness, the intervariant boundaries were further categorized into block, sub-block and packet boundaries according to the boundary types [13,15], and the densities of the intervariant boundaries were calculated. As shown in Figure 6a, the head exhibits a significantly higher density of block boundaries from different Bain groups than the end, which is a result of its weaker variant selection [8,36]. Previous studies have shown that a lower starting temperature of transformation can be triggered by a higher cooling rate, and thus a greater driving force for phase transformation can be obtained [8,35,37]. In this work, the higher cooling rate in the head provided a greater driving force, more variants from distinct Bain groups formed and the block width became finer, thus accommodating greater transformation strain [15,38,39]. Figure 6b summarizes the boundary density and impact toughness. The density of block boundaries shows a similar tendency with that of the impact toughness, suggesting that a HAGB dominated by block boundaries is the key factor affecting the toughness, consistent with the results in refs. [9,27,40–42]. Therefore, the high cooling rate in the head weakened the variant selection, resulting in the high density of block boundaries and impact toughness.
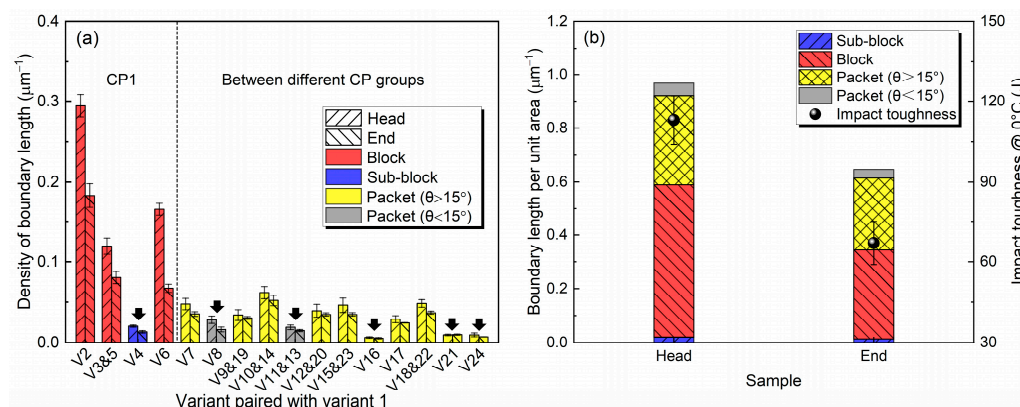

Figure 6. Density of intervariant boundaries (**a**) and relationship between boundary density and impact toughness (**b**) of the samples. Black arrows point out the intervariant relations belonging to the same Bain group.

4. Conclusions

The mechanism responsible for the toughness fluctuation in ultra-high-strength casings was elucidated from the aspect of crystallography. The head of the casing exhibits a higher impact toughness and density of HAGBs dominated by block boundaries and weaker variant selection compared with the end. The variation in the impact toughness between the head and the end is related to the different cooling rates along the casing. The high cooling rate at the head can provide a large driving force and weaken the variant selection, which results in the high density of block boundaries and impact toughness. Thus, the varying density of block boundaries provoked by uneven cooling is responsible for toughness fluctuations in the casing.

Data Availability Statement: The data presented in this study are available on request from the corresponding author due to legal and ethical reasons.

Conflicts of Interest: Z.G. and X.D. were employed by the Baoshan Iron & Steel Co., Ltd. The remaining authors declare that the research was conducted in the absence of any commercial or financial relationships that could be construed as a potential conflict of interest.

References

1. Li, H.; Han, L.; Zhang, W. Demand for and development of hi-performance OCTG. *Steel Pipe* **2009**, *38*, 1–9. [CrossRef]
2. Feng, Y.; Li, H.; Han, L.; Zhang, Z.; Zhang, C.; Cheng, H.; Bai, Z.; Tian, Y.; Shi, X.; Xie, J.; et al. Progress and prospects of manufacturing technology for oil country tubular goods in China. *Pet. Sci. Bull.* **2022**, *7*, 229–241. [CrossRef]
3. Chen, H.; Yu, Y.S.; Wu, B.B.; Shang, C.J. Metallurgical design and high strength-toughness mechanism of ultrahigh strength-toughness oil pipeline steel. *Kang T'ieh/Iron Steel* **2019**, *54*, 96–103. [CrossRef]
4. Costa e Silva, A.L.V.d. Non-metallic inclusions in steels—Origin and control. *J. Mater. Res. Technol.* **2018**, *7*, 283–299. [CrossRef]
5. Liu, Z.P.; Xie, Z.J.; Luo, D.; Zhou, W.H.; Guo, H.; Shang, C.J. Influence of central segregation on the welding microstructure and properties of FH40 cryogenic steel. *Gongcheng Kexue Xuebao/Chin. J. Eng.* **2023**, *45*, 1335–1341. [CrossRef]
6. Han, P.; Liu, Z.; Xie, Z.; Wang, H.; Jin, Y.; Wang, X.; Shang, C. Influence of band microstructure on carbide precipitation behavior and toughness of 1 GPa-grade ultra-heavy gauge low-alloy steel. *Int. J. Miner. Metall. Mater.* **2023**, *30*, 1329–1337. [CrossRef]
7. Xiong, Z.; Liu, S.; Wang, X.; Shang, C.; Misra, R.D.K. Relationship between crystallographic structure of the Ti_2O_3/MnS complex inclusion and microstructure in the heat-affected zone (HAZ) in steel processed by oxide metallurgy route and impact toughness. *Mater. Charact.* **2015**, *106*, 232–239. [CrossRef]
8. Yu, H.; Yu, Y.; Wang, Z.; Li, F.; Hu, B.; Liu, S. On the variant pairing in transformation product of high strength low alloy steel depending on cooling rate. *Mater. Lett.* **2022**, *326*, 132953. [CrossRef]
9. Liu, Z.C.; Wang, X.L.; Yu, Y.S.; Shang, C.J. Study on toughening mechanism of high strength steel and its relationship with substructure. *J. Iron Steel Res.* **2020**, *32*, 1093–1101. [CrossRef]
10. Bai, P.; Shang, C.; Wu, H.-H.; Ma, G.; Wang, S.; Wu, G.; Gao, J.; Chen, Y.; Zhang, J.; Zhu, J.; et al. A review on the advance of low-temperature toughness in pipeline steels. *J. Mater. Res. Technol.* **2023**, *25*, 6949–6964. [CrossRef]
11. Huang, S.; Yu, Y.S.; Wang, Z.Q.; Su, S.; Chen, K.; Yuan, S.F.; Xie, Z.J.; Shang, C.J. Crystallographic insights into the role of nickel on hardenability of wear-resistant steels. *Mater. Lett.* **2022**, *306*, 130961. [CrossRef]
12. Chen, Q.-Y.; Zhang, W.-N.; Wang, P.-J.; Mao, Q.-J.; Liu, Z.-Y. Crystallography of transformation products with different cooling rates in low-carbon alloy steel and its effect on low-temperature toughness uniformity of heavy plates. *J. Mater. Res. Technol.* **2024**, *28*, 2077–2085. [CrossRef]

13. Morito, S.; Tanaka, H.; Konishi, R.; Furuhara, T.; Maki, T. The morphology and crystallography of lath martensite in Fe-C alloys. *Acta Mater.* **2003**, *51*, 1789–1799. [CrossRef]
14. Morito, S.; Huang, X.; Furuhara, T.; Maki, T.; Hansen, N. The morphology and crystallography of lath martensite in alloy steels. *Acta Mater.* **2006**, *54*, 5323–5331. [CrossRef]
15. Takayama, N.; Miyamoto, G.; Furuhara, T. Effects of transformation temperature on variant pairing of bainitic ferrite in low carbon steel. *Acta Mater.* **2012**, *60*, 2387–2396. [CrossRef]
16. Luo, H.; Wang, X.; Liu, Z.; Yang, Z. Influence of refined hierarchical martensitic microstructures on yield strength and impact toughness of ultra-high strength stainless steel. *J. Mater. Sci. Technol.* **2020**, *51*, 130–136. [CrossRef]
17. Morris, J.J.W.; Lee, C.S.; Guo, Z. The Nature and Consequences of Coherent Transformations in Steel. *ISIJ Int.* **2003**, *43*, 410–419. [CrossRef]
18. Wang, C.; Wang, M.; Shi, J.; Hui, W.; Dong, H. Effect of microstructural refinement on the toughness of low carbon martensitic steel. *Scr. Mater.* **2008**, *58*, 492–495. [CrossRef]
19. Chatterjee, A.; Chakrabarti, D.; Moitra, A.; Mitra, R.; Bhaduri, A.K. Effect of deformation temperature on the ductile–brittle transition behavior of a modified 9Cr–1Mo steel. *Mater. Sci. Eng. A* **2015**, *630*, 58–70. [CrossRef]
20. Li, X.C.; Zhao, J.X.; Cong, J.H.; Misra, R.D.K.; Wang, X.M.; Wang, X.L.; Shang, C.J. Machine learning guided automatic recognition of crystal boundaries in bainitic/martensitic alloy and relationship between boundary types and ductile-to-brittle transition behavior. *J. Mater. Sci. Technol.* **2021**, *84*, 49–58. [CrossRef]
21. *GB/T 228.1-2021*; Metallic Materials—Tensile Testing—Part I: Method of Test at Room Temperature. China Standard Press: Beijing, China, 2021.
22. *GB/T 229−2020*; Metallic Materials—Charpy Pendulum Impact Test Method. China Standard Press: Beijing, China, 2020.
23. Huang, S.; Wu, B.B.; Wang, Z.Q.; Yu, Y.S.; Wang, C.S.; Yan, L.; Li, X.C.; Shang, C.J.; Misra, R.D.K. EBSD study on the significance of carbon content on hardenability. *Mater. Lett.* **2019**, *254*, 412–414. [CrossRef]
24. Li, X.; Zhao, J.; Wang, J.; Wang, X.; Liu, S.; Shang, C. Effect of boundaries on toughness in high-strength low-alloy steels from the view of crystallographic misorientation. *Mater. Lett.* **2020**, *259*, 126841. [CrossRef]
25. Gourgues, A.F. Electron backscatter diffraction and cracking. *Mater. Sci. Technol.* **2002**, *18*, 119–133. [CrossRef]
26. Li, X.; Zhao, J.; Dong, L.; Devesh Kumar Misra, R.; Wang, X.; Wang, X.; Shang, C. The significance of coherent transformation on grain refinement and consequent enhancement in toughness. *Materials* **2020**, *13*, 5095. [CrossRef]
27. Yu, Y.-S.; Wang, Z.-Q.; Wu, B.-B.; Zhao, J.-X.; Wang, X.-L.; Guo, H.; Shang, C.-J. Tailoring variant pairing to enhance impact toughness in high-strength low-alloy steels via trace carbon addition. *Acta Metall. Sin.* **2021**, *34*, 755–764. [CrossRef]
28. Fan, E.; Li, Y.; You, Y.; Lü, X. Effect of crystallographic orientation on crack growth behaviour of HSLA steel. *Int. J. Miner. Metall. Mater.* **2022**, *29*, 1532–1542. [CrossRef]
29. Yu, Y.S.; Wang, Z.Q.; Wu, B.B.; Rong, X.Q.; Wei, L.J.; Yuan, S.F.; Guo, H.; Shang, C.J. New insight into the hardenability of high strength low alloy steel from the perspective of crystallography. *Mater. Lett.* **2021**, *292*, 129624. [CrossRef]
30. Ståhlkrantz, A.; Hedström, P.; Sarius, N.; Borgenstam, A. Effect of carbon content on variant pairing in bainitic low alloy steel. *Metall. Mater. Trans. A* **2022**, *53*, 3418–3427. [CrossRef]
31. Wang, B.; Chen, N.; Cai, Y.; Guo, W.; Wang, M. Effect of crystallographic features on low-temperature fatigue ductile-to-brittle transition for simulated coarse-grained heat-affected zone of bainite steel weld. *Int. J. Fatigue* **2023**, *170*, 107523. [CrossRef]
32. Yin, T.W.; Shen, Y.F.; Jia, N.; Li, Y.J.; Xue, W.Y. Controllable selection of martensitic variant enables concurrent enhancement of strength and ductility in a low-carbon steel. *Int. J. Plast.* **2023**, *168*, 103704. [CrossRef]
33. Miyamoto, G.; Takayama, N.; Furuhara, T. Accurate measurement of the orientation relationship of lath martensite and bainite by electron backscatter diffraction analysis. *Scr. Mater.* **2009**, *60*, 1113–1116. [CrossRef]
34. Miyamoto, G.; Iwata, N.; Takayama, N.; Furuhara, T. Mapping the parent austenite orientation reconstructed from the orientation of martensite by EBSD and its application to ausformed martensite. *Acta Mater.* **2010**, *58*, 6393–6403. [CrossRef]
35. Wu, B.B.; Wang, Z.Q.; Yu, Y.S.; Wang, X.L.; Shang, C.J.; Misra, R.D.K. Thermodynamic basis of twin-related variant pair in high strength low alloy steel. *Scr. Mater.* **2019**, *170*, 43–47. [CrossRef]
36. Liu, Z.; Yu, Y.; Yang, J.; Wang, Z.; Guo, H.; Shang, C. Morphology and crystallography analyses of HSLA steels with hardenability enhanced by tailored C–Ni collocation. *Metals* **2022**, *12*, 32. [CrossRef]
37. Long, X.; Liu, W.; Zhu, R.; Zhang, Y.; Zhang, F.; Yang, Z.; Li, Y. Effect of the cooling rate in the medium temperature zone on the phase transformation and microstructure of carbide-free bainitic steel. *J. Mater. Res. Technol.* **2024**, *29*, 50–66. [CrossRef]
38. Kawata, H.; Sakamoto, K.; Moritani, T.; Morito, S.; Furuhara, T.; Maki, T. Crystallography of ausformed upper bainite structure in Fe–9Ni–C alloys. *Mater. Sci. Eng. A* **2006**, *438–440*, 140–144. [CrossRef]
39. Xi, X.; Wu, T.; Wang, S.; Wang, J.; Wang, G.; Chen, L. Research on the mechanism of Cu addition on the grain boundary characteristics and toughness in CGHAZ of low carbon low alloy steel. *J. Mater. Res. Technol.* **2023**, *23*, 577–586. [CrossRef]
40. Li, X.; Lu, G.; Wang, Q.; Zhao, J.; Xie, Z.; Misra, R.D.K.; Shang, C. The effects of prior austenite grain refinement on strength and toughness of high-strength low-alloy steel. *Metals* **2022**, *12*, 28. [CrossRef]

41. Wang, X.L.; Xie, Z.J.; Wang, Z.Q.; Yu, Y.S.; Wu, L.Q.; Shang, C.J. Crystallographic study on microstructure and impact toughness of coarse grained heat affected zone of ultra-high strength steel. *Mater. Lett.* **2022**, *323*, 132552. [CrossRef]
42. Qi, X.; Huan, P.; Wang, X.; Di, H.; Shen, X.; Sun, Q.; Liu, Z.; He, J. Study on the mechanism of heat input on the grain boundary distribution and impact toughness in CGHAZ of X100 pipeline steel from the aspect of variant. *Mater. Charact.* **2021**, *179*, 111344. [CrossRef]